

1

2           **Submesoscales are a significant turbulence source in global**  
3                                   **ocean surface boundary layer**

4

5     Jihai Dong<sup>1,2</sup>, Baylor Fox-Kemper<sup>3</sup>, Jacob O. Wenegrat<sup>4</sup>, Abigail S. Bodner<sup>5</sup>, Hong Zhang<sup>6</sup>,  
6     Xiaolong Yu<sup>7</sup>, Changming Dong<sup>1,2</sup>

7     <sup>1</sup>School of Marine Sciences, Nanjing University of Information Science and Technology, Nanjing,  
8     China

9     <sup>2</sup>Southern Marine Science and Engineering Guangdong Laboratory (Zhuhai), Zhuhai, China,

10    <sup>3</sup>Department of Earth, Environmental, and Planetary Sciences, Brown University, Providence,  
11    Rhode Island, USA

12    <sup>4</sup>Department of Atmospheric and Oceanic Science, University of Maryland, College Park, College  
13    Park, Maryland, USA

14    <sup>5</sup>The Center for Atmosphere Ocean Science, New York University, New York City, New York,  
15    USA

16    <sup>6</sup>Jet Propulsion Laboratory, California Institute of Technology, Pasadena, California, USA

17    <sup>7</sup>School of Marine Sciences, Sun Yat-sen University, Zhuhai, China

18

19    **Keywords:** ocean surface boundary layer; turbulent mixing; Langmuir turbulence; front;  
20    submesoscale

21

22

23 **Abstract**

24 The turbulent ocean surface boundary layer is a key part of the climate system affecting both the  
25 energy and carbon cycles. Accurately simulating the boundary layer is critical in improving climate  
26 model performance, which deeply relies on our understanding of the turbulence in the boundary  
27 layer. Turbulent energy sources in the boundary layer are traditionally believed to be dominated  
28 by waves, winds and convection. Recently, submesoscale phenomena with spatial scales of  
29 0.1~10 km at ocean fronts have been shown to also make a contribution. However, the global  
30 contribution of energy transfer by submesoscales at fronts was unclear. By recalibrating the  
31 outputs from a submesoscale-permitting global model based on theory predicting the frontal  
32 arrest scale, we show that the submesoscale geostrophic shear production at fronts is a  
33 significant turbulent energy source within the ocean boundary layer, contributing 34% to the total  
34 dissipation in winter and 17% in summer, despite its intermittency in space and time. This work  
35 indicates fundamental deficiencies in previous conceptions of ocean boundary layer turbulence,  
36 and invites a reappraisal of the sampling scale in observations, model resolution and  
37 parameterizations, and other consequences of the global energy budget.

38  
39 **Introduction**

40  
41 The ocean surface boundary layer (OSBL), a turbulent upper layer in the ocean, provides the  
42 channel for the atmosphere to communicate with the ocean interior. Intense air-sea exchanges of  
43 momentum and heat energize small-scale (<100 m) turbulence and make the OSBL the most  
44 turbulent layer in the ocean<sup>1</sup>. OSBL turbulence modulates the transfer of momentum, heat and  
45 dissolved gases between the sea surface and ocean interior. These exchanges affect the water  
46 properties of the ocean, thereby influencing climate variability on timescales from days to  
47 centuries<sup>2, 3, 4, 5, 6</sup>. Turbulence also enhances the upward flow of nutrients to the light-filled  
48 biologically-productive layers, a control on primary ocean productivity<sup>7, 8</sup>. OSBL turbulence is not  
49 resolved in most ocean and climate models and is usually represented by parameterizations.

50  
51 Studies in the last decades have been conducted to quantify the contributions from OSBL  
52 processes including winds, waves, and convection<sup>9, 10, 11</sup> to OSBL turbulence. These prior  
53 assessments focused only on the sources of turbulent kinetic energy (TKE) that are effectively  
54 one-dimensional—consistent with classical conceptions of boundary layer turbulence and easily  
55 determined by the available data and models. Extensive work has now documented that OSBL  
56 turbulence can be significantly altered in frontal regions with strong vertical shears providing a  
57 significant source of TKE via submesoscale phenomena with spatial scales of 0.1~10km<sup>12</sup>.  
58 Observations also show that classical scalings of OSBL turbulence are deficient<sup>13, 14</sup>, while a  
59 significant contribution of fronts to OSBL turbulence has been reported<sup>15, 16, 17</sup>. This geostrophic  
60 shear turbulence (GSP) source due to submesoscales relies on horizontal buoyancy gradients  
61 and is therefore fundamentally informed by two-dimensional flow parameters. This mixing is  
62 important for both vertical and horizontal exchange of properties at ocean fronts, but is not  
63 included in prior global assessments of OSBL turbulence, nor currently widely-used  
64 parameterizations<sup>18, 19</sup>.

65  
66 In this work, GSP is found to be a significant, yet highly intermittent, contributor to global OSBL  
67 turbulence. To show this we extend the Belcher et al.<sup>10</sup> approach to determining sources of TKE  
68 production by surface forcing to include GSP contributions, and we compare the relative  
69 significance of four kinds of turbulence: geostrophic shear production turbulence at fronts (GSP),  
70 Langmuir shear production turbulence due to waves (LSP), ageostrophic shear production  
71 turbulence due to surface wind stress (AGSP) and vertical buoyancy production turbulence due to  
72 surface buoyancy loss (VBP) in the global OSBL. GSP is found to be a leading contributor to  
73 turbulence in the OSBL and the prevalent one in winter. The result is robust to the analysis  
74 choices, and provides a clue to reasons for the OSBL bias in ocean and climate model  
75 simulations and a direction to improve model capability for climate change projections.

76

77 **Results**

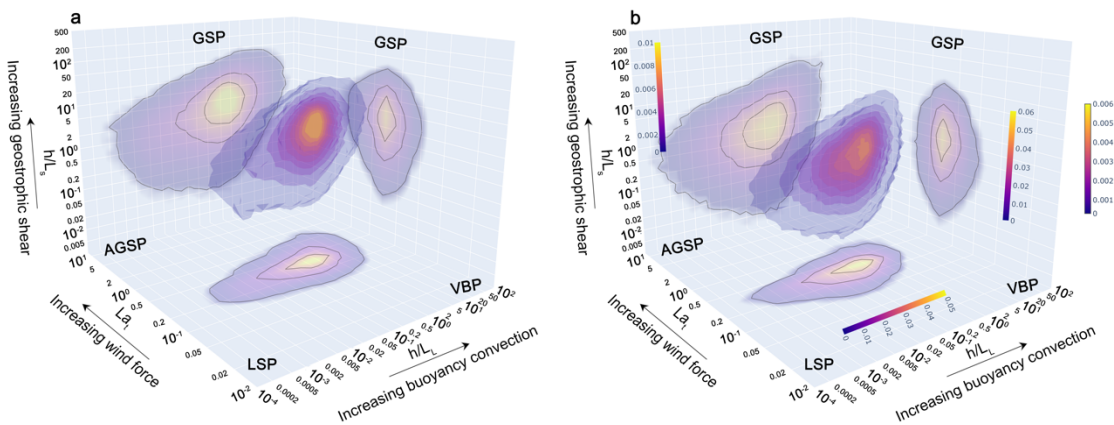
78

79 **Distributions of the turbulence sources**

80 The relative contributions of four sources of turbulence, waves (LSP), fronts (GSP), surface  
 81 buoyancy loss (VBP) and wind (AGSP) to OSBL turbulence are determined by three non-  
 82 dimensional parameters, the turbulent Langmuir number  $La_t$ , the ratio of the boundary layer  
 83 depth to the Langmuir stability length  $h/L_L$ , and the ratio of the boundary layer depth to the  
 84 geostrophic shear stability length  $h/L_s$  (**Methods**). The relative importance of wind forcing, waves,  
 85 buoyancy convection and geostrophic shear are reflected by location along the three axes of the  
 86 plots in **Fig. 1**.  
 87

88  $La_t$  of the x-axis governs the wind-forced turbulence source (AGSP) against the wave-forced  
 89 turbulence source (LSP), and LSP dominates over AGSP when  $La_t < 0.3$ <sup>10</sup>. The global  
 90 distribution of  $La_t$  shows seasonality of LSP and AGSP consistent with that found in Belcher et al.  
 91 <sup>10</sup>. The parameter  $h/L_L$  of the y-axis measures the source of convective turbulence (VBP) against  
 92 LSP. Large  $h/L_L$  values ( $h/L_L > 1$ ) indicate a dominant role of VBP over LSP. This ratio is much  
 93 larger in winter (generally  $> 1$ ), implying a generally more dominant role of LSP over VBP.  
 94

95 To measure the relative GSP magnitude, the ratio  $h/L_s$  is used<sup>20</sup>. The geostrophic shear stability  
 96 length  $L_s$  depends on the strength of horizontal buoyancy gradients associated with fronts.  
 97 Estimation of this quantity requires a rescaling of the resolved model buoyancy gradients, which  
 98 is done assuming frontal arrest under the Turbulent Thermal Wind balance (TTW; **Methods**)<sup>21</sup>,  
 99 although we emphasize that major results are qualitatively robust to this choice as assessed  
 100 below. Much of the estimated global distribution is characterized by  $h/L_s > 1$  in the z-axis,  
 101 indicating the frontal contribution to TKE production (GSP) dominates over wind-forced  
 102 turbulence (AGSP). Seasonal variation of  $h/L_s$  is also significant, with larger  $h/L_s$  values in winter  
 103 resulting from more active submesoscale fronts with intense horizontal density gradients<sup>22</sup> that  
 104 outpace the enhanced AGSP associated with winter storms.  
 105



106

107 **Fig. 1 Three-dimensional global probability density of the three parameters. a**, The  
 108 probability density in winter. **b**, The probability density in summer. The three parameters are  
 109 turbulent Langmuir number  $La_t$  of the x-axis, the ratio of the boundary layer depth to the Langmuir  
 110 stability length  $h/L_L$  of the y-axis, and the ratio of the boundary layer depth to the geostrophic  
 111 shear stability length  $h/L_s$  of the z-axis. Two-dimensional projections of the distributions are also  
 112 shown. The black contours enclose 30%, 60%, and 90% of the global values. Each source of  
 113 turbulence is labeled and the contribution of fronts (GSP) is highlighted as the geostrophic shear  
 114 along the z-axis is increased.  
 115

116

**Dissipation regimes in parameter space**

117 Two-dimensional probability distribution slices overlapped on regime maps derived from **Fig. 1**  
118 are shown (**Fig. 2**). The  $La_t$ - $h/L_L$  projection, neglecting the geostrophic shear, has been discussed  
119 by Belcher et al. and Li et al.<sup>10,11</sup> who argued for a significant role of LSP in generating OSBL  
120 turbulence. As the parameter  $h/L_s$  is introduced, the regimes are changed. The percentiles  
121 indicate that the global OSBL is generally under LSP and LSP/VBP regimes for locations with  
122 weak geostrophic shears (**Fig. 2a**). GSP begins to play a role while LSP and AGSP are  
123 weakened as the geostrophic shear increases (**Fig. 2d,g**).

124

125 The  $La_t$ - $h/L_s$  space shows the dependence of the regimes on buoyancy convection. When the  
126 surface buoyancy convection is weak, the enclosed contours show that most of the locations are  
127 dominated by LSP, GSP and their mixed regime, indicating an important role of GSP globally in  
128 these conditions (**Fig. 2b**). The contribution of LSP turbulence is finally eliminated as the surface  
129 buoyancy loss continues to increase, and GSP and VBP dominate OSBL turbulence (**Fig. 2e,h**).

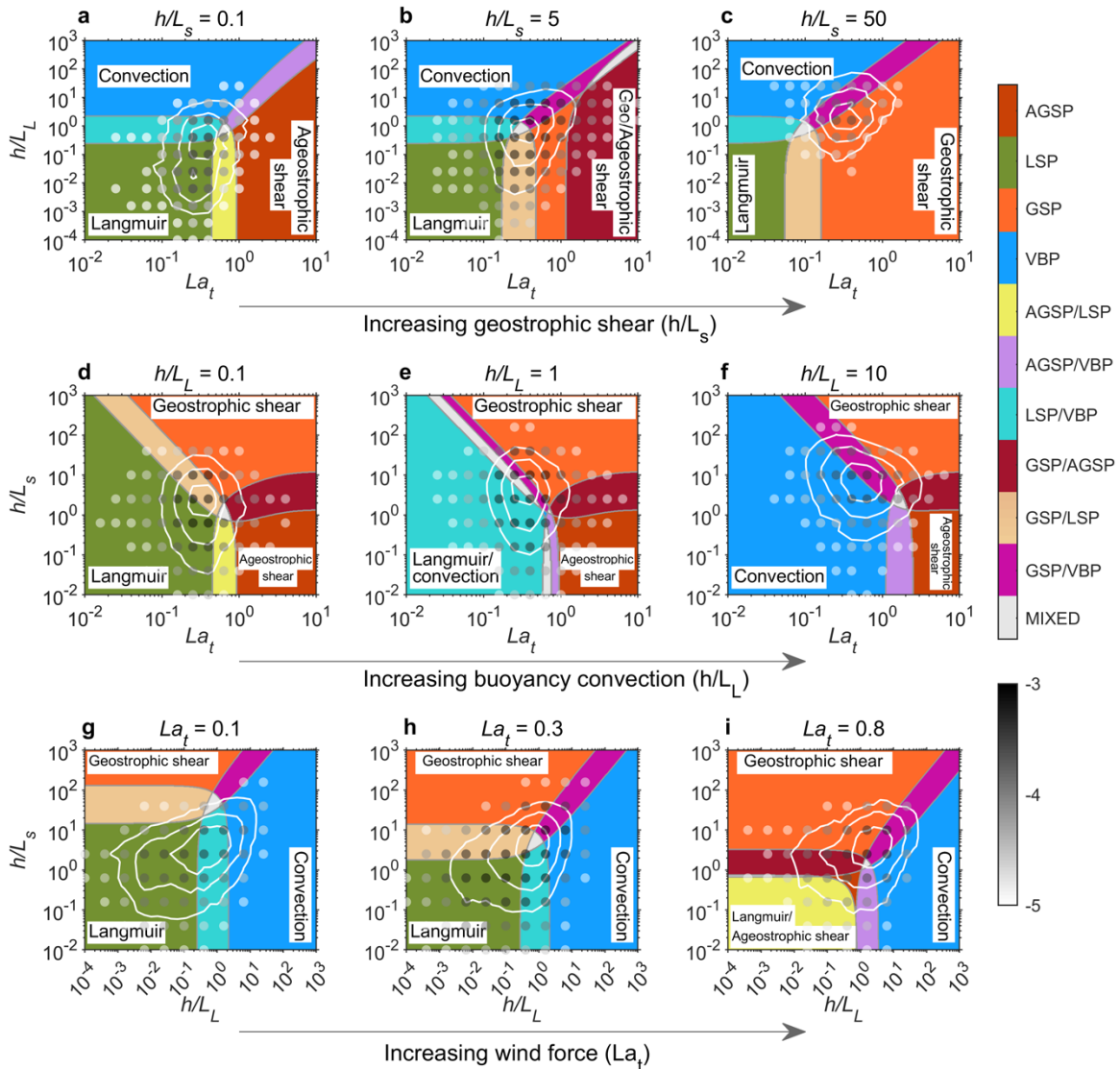
130

131 In the  $h/L_L$ - $h/L_s$  space, LSP and VBP dominate OSBL turbulence when  $La_t$  is small (**Fig. 2c**). The  
132 percentile distributions show that almost 90% of the locations with small  $La_t$  are dominated by  
133 LSP, VBP and their mixed regimes. As the wind forcing becomes stronger, the contribution from  
134 LSP is decreased but GSP and AGSP become more important. When the wind forcing is  
135 sufficiently strong, more than 90% of the corresponding locations are under a mix of AGSP, GSP,  
136 VBP (**Fig. 2i**).

137

138 In summer, as the wind force, buoyancy loss and geostrophic shear are all weakened, the  
139 distributions of these parameters are shifted to small values (**Fig. S1**). The role of LSP is  
140 generally strengthened, while other turbulence sources are weakened. In particular, the relative  
141 importance of GSP is weakened from winter to summer, which is the opposite behavior of LSP.

142



143  
144  
145  
146  
147  
148  
149  
150  
151  
152  
153  
154  
155  
156  
157  
158  
159  
160  
161

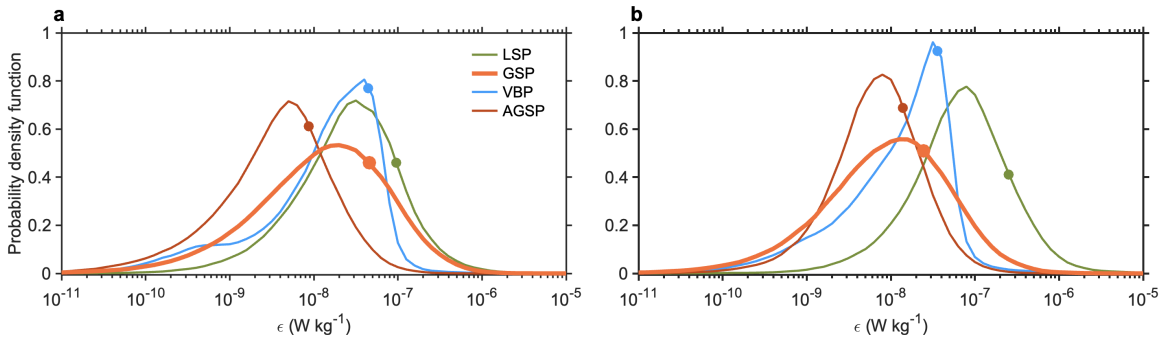
**Fig. 2** Turbulence regimes in parameter slices in winter. **a**,  $h/L_s=0.1$ . **b**,  $h/L_s=5$ . **c**,  $h/L_s=50$ . **d**,  $h/L_L=0.1$ . **e**,  $h/L_L=1$ . **f**,  $h/L_L=10$ . **g**,  $La_t=0.1$ . **h**,  $La_t=0.3$ . **i**,  $La_t=0.8$ . The regimes are defined by the dominant production terms in the TKE budget. The white contours enclose 30%, 60%, and 90% of the locations with the corresponding values. A regime is considered dominant when its contribution exceeds 75% of the total dissipation, otherwise, it is a two-turbulence-mixed regime when two TKE sources both contribute more than 25% while all others contribute less than 25%, and lastly, it is a mixed regime if more than three sources of turbulence contribute more than 25%. The dots denote the possibility density (in logarithm with 10-base) along these slices from **Fig. 1**. The distributions indicate that GSP is an important regime for OSBL turbulence over the globe, especially at locations with strong frontal geostrophic shears.

### Dissipation magnitudes globally

According to both mean and median absolute dissipation rates, LSP has the largest magnitude in both seasons (**Fig. 3**; **Fig. S2**). The dominant role of LSP has been reported by previous studies<sup>10,11</sup>. Without considering GSP, Li et al.<sup>11</sup> found the OSBL is dominated by LSP (e.g., the Southern Ocean), or VBP (e.g., tropical regions), and mixed LSP and VBP (i.e., mid-latitude regions). By contrast, GSP is here shown to often be larger than the VBP and AGSP

162 contributions, and to rival LSP in winter. GSP is stronger in winter, especially so in the western  
 163 boundary currents and the Southern Ocean. Overall, the relative contributions of GSP to the total  
 164 dissipation averaged over the globe are 35% in winter and 18% in summer.

165  
 166 Probability density functions (PDFs) of all turbulence sources show nearly log-skew-normal  
 167 distributions (**Fig. 3**), consistent with both intermittent alternating energy sources<sup>23</sup> and the  
 168 forward cascade of oceanic turbulence<sup>24</sup>. In such distributions, the large mean rates are  
 169 determined by intermittent extreme events, rather than the accumulation. Compared with the  
 170 other sources, GSP has the widest distribution, implying it has the highest intermittency and the  
 171 greatest difference between its average and median values. This highlights a challenge in  
 172 observational estimates of integrated contributions of frontal turbulence. Extremely sharp fronts,  
 173 while covering very limited spatial extent and oftentimes being transient, can be associated with  
 174 sufficiently large GSP so as to significantly influence the mean values.  
 175



176  
 177 **Fig. 3 PDFs of the turbulence sources.** **a**, PDFs of the four sources in winter. **b**, PDFs of the  
 178 four sources in summer. The dots indicate the corresponding global mean value of each  
 179 distribution. The log-normal distribution of the PDFs suggests that the mean and integral of OSBL  
 180 dissipation are determined by intermittent high dissipation rates. The highest intermittency of GSP  
 181 can also be derived from the distributions.  
 182  
 183

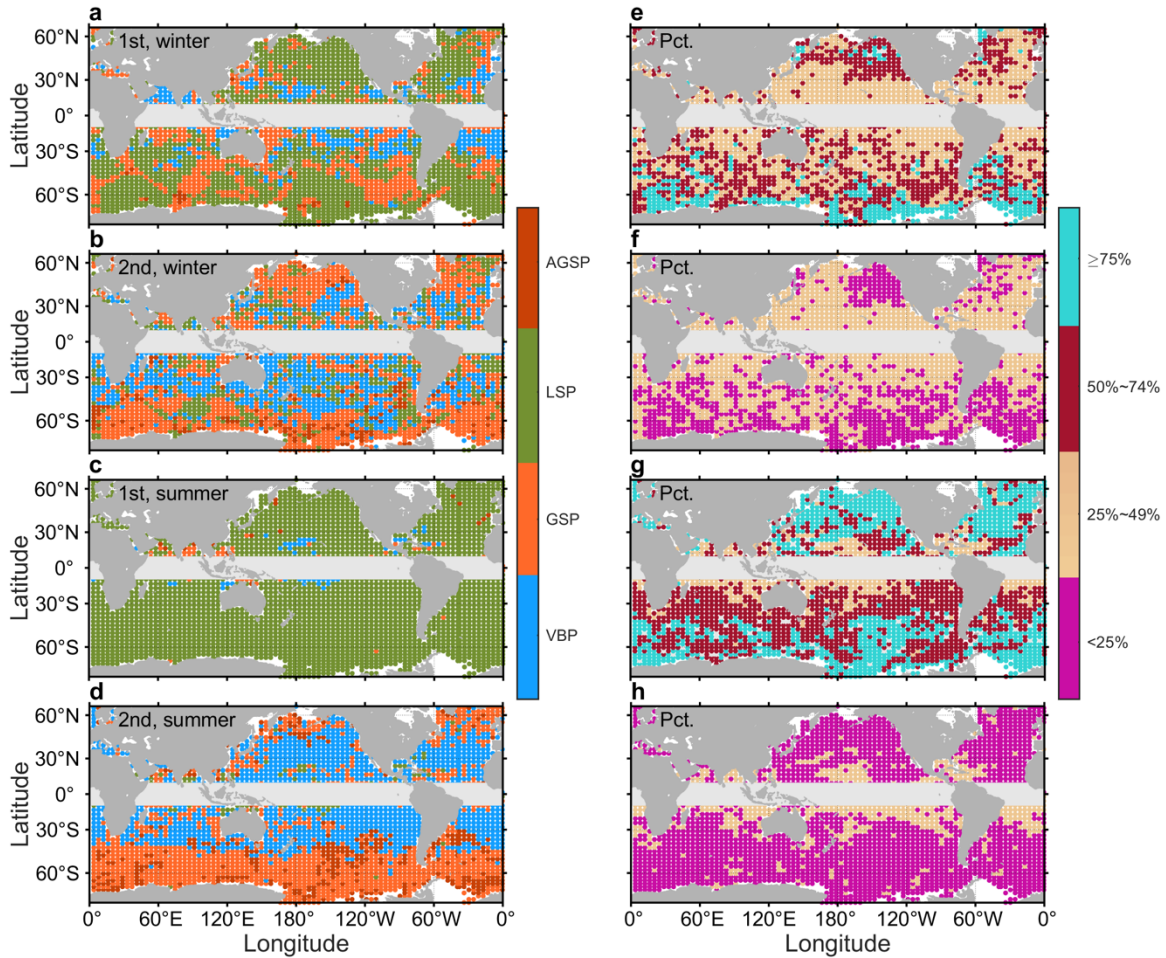
### 184 Turbulent energy sources globally

185 The spatial distribution of the global turbulence sources can be determined by ranking the relative  
 186 contributions of the four sources by location. **Fig. 4** maps the top two turbulence sources over the  
 187 globe and the associated contributions relative to the total dissipation in different seasons. In  
 188 winter, LSP is the most spatially prevalent source, accounting for 44% of the global locations,  
 189 especially at mid and high latitudes (**Fig. 4a**). The spatial prevalence of GSP is 37% and is most  
 190 common at low and mid latitudes, while some locations at low latitudes are controlled by VBP  
 191 (16% of all locations). A latitudinal dependence in the percentage contribution of the principal  
 192 source is evident, with the largest source generally contributing less than 50% of the total  
 193 dissipation at low latitudes, growing to larger than 75% at high latitudes. The contribution of VBP  
 194 (35%) and GSP (34%) become the most dominant regimes in the map of the secondary sources  
 195 (**Fig. 4b**).  
 196

197 Overall, considering the top two sources, GSP is the most spatially extensive primary source,  
 198 providing a leading contribution to turbulence in 71% of the locations considered. By contrast, it is  
 199 70% for LSP and 51% for VBP. Moreover, the relative contribution of GSP explicitly shows where  
 200 GSP dominates OSBL turbulence, such as the western North Pacific Ocean, the Eastern North  
 201 Atlantic Ocean in winter, and the Southern Ocean in both seasons (**Fig. S3**). Thus, while  
 202 individual sharp fronts cover very limited spatial area, their contribution to OSBL turbulence may  
 203 have broad impact.  
 204



205 In summer the distribution of energy sources changes, consistent with changes in surface forcing  
 206 and the known seasonality of submesoscale turbulence<sup>22, 25, 26</sup>. LSP is the most spatially-  
 207 prevalent source over the globe, except for a few tropical regions with significant GSP and VBP  
 208 contributions. LSP accounts for 84% of all summer locations, much larger than other sources  
 209 (11% for GSP and 4% for VBP). This dominance is highlighted by the relative contribution shown  
 210 in **Fig. 4g**, which indicates that the LSP may be responsible for more than 50% of global OSBL  
 211 turbulence production outside of the tropics. For the second dominant sources, it is GSP at high  
 212 latitudes while VBP at low latitudes (**Fig. 4d**).  
 213



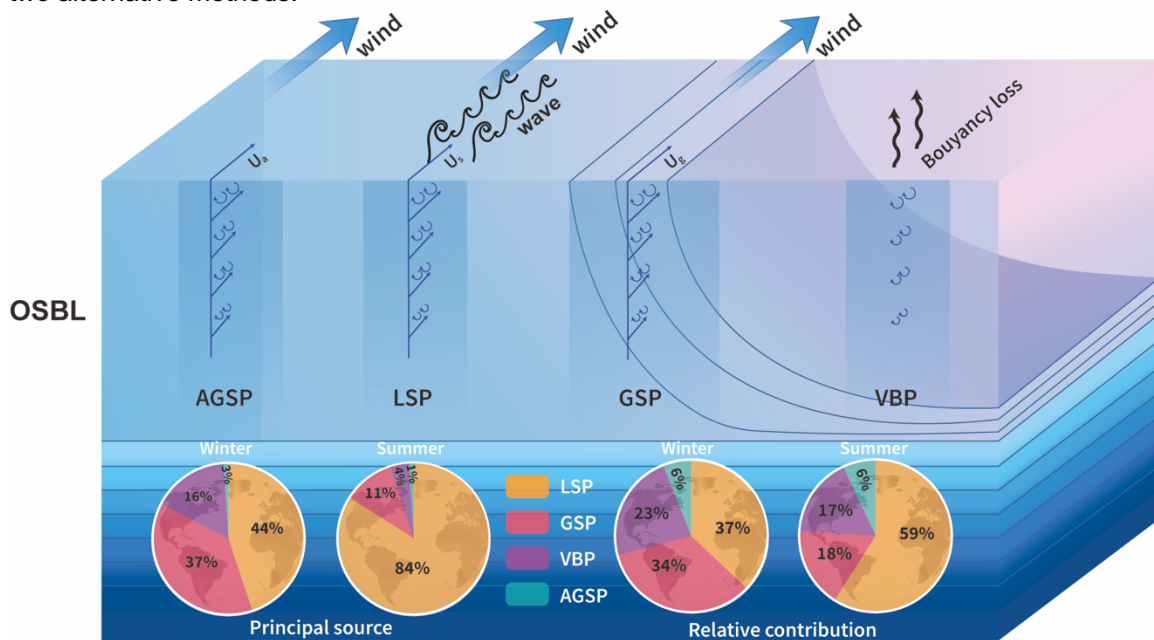
214 **Fig. 4. Global distributions of the two most likely dominant sources at each location.** **a**, The  
 215 first most likely dominant sources in winter. **b**, The second most likely dominant sources in winter.  
 216 **c**, The first most likely dominant sources in summer. **d**, The second most likely dominant sources  
 217 in summer. Their relative contribution percentages to the total mean dissipation (%) are shown in  
 218 **e-h**. The relative contributions shown in **e-h** indicate that the summation of the top two sources  
 219 can explain most ( $Pct_{1st} + Pct_{2nd} > 55\%$ ) of the total dissipation. GSP turbulence is the first largest  
 220 contributor at low and mid latitudes in winter, and still the second largest contributor at high  
 221 latitudes in both seasons.  
 222

223

## 224 Discussion

225 The results here suggest that ocean fronts make a leading-order contribution to OSBL turbulence  
 226 in many parts of the global ocean. This result differs fundamentally from classic conceptual  
 227 models assuming horizontally uniform flows, and it implies parameterizations of OSBL turbulence  
 228 that account only for wind, wave, and convective sources of turbulence are deficient. A schematic

229 diagram of the four kinds of turbulence sources and their relative contributions is shown in **Fig. 5**.  
 230 Nevertheless, its quantitative estimation heavily relies on the robustness of the calculation of the  
 231 horizontal buoyancy gradient. Here the robustness of these results is also tested by using other  
 232 two alternative methods.



233 **Fig. 5 A schematic diagram of the four turbulence sources.** LSP, GSP, VBP, and AGSP  
 234 represent the turbulence sources from Langmuir circulation, geostrophic current shear, vertical  
 235 convection, and ageostrophic current shear. LSP is the shear to turbulence from Stokes drifts due  
 236 to winds and waves. GSP is the shear to turbulence from geostrophic currents at fronts with  
 237 down-front winds. VBP is the convection to turbulence by gravitational instability due to surface  
 238 buoyancy loss. AGSP is the shear to turbulence from ageostrophic currents induced by winds.  
 239 The left two pie charts show the spatial prevalence of each turbulence source in winter and  
 240 summer, while the right two show the relative contribution of each source to the total dissipation  
 241 magnitude averaged over the globe. These percentages indicate that GSP is a prevalent and  
 242 significant source of OSBL turbulence over the globe.  
 243  
 244

245  
 246 First, GSP is calculated based directly on the raw resolved buoyancy gradients of the numerical  
 247 model (“uncorrected” method). These estimates can therefore be thought of as a conservative  
 248 lower bound<sup>21, 27</sup>. Second, we rescale the buoyancy gradients by assuming a horizontal  
 249 buoyancy density gradient spectrum consistent with white noise from the effective resolution  
 250 down to the frontal arrest scale (“no-slope” method)<sup>28</sup>. This approach leads to a larger estimate  
 251 of the horizontal buoyancy gradient (or smaller  $L_s$ ), and thus provides an upper bound of GSP  
 252 dissipation.  
 253

254 Unsurprisingly, the role of GSP is weakened for the uncorrected case, while it is strengthened for  
 255 the no-slope case (**Fig. S4 and S5**). Taking the uncorrected and no-slope estimates as effective  
 256 upper and lower uncertainty bounds, the mean relative contributions of GSP are 34% with the  
 257 uncertainty of [27%, 37%] in winter and 17% [16%, 18%] in summer. The dominant locations for  
 258 each energy source and their averages and percentiles (**Tab. S1**) indicate that GSP still emerges  
 259 as a major global source of TKE in the boundary layer even when using the most conservative  
 260 approach of estimating the horizontal buoyancy gradient directly from the marginally  
 261 submesoscale-permitting  $1/48^\circ$  model run solution, suggesting the robust role of fronts in  
 262 energizing global boundary layer turbulence.



263 The turbulence sources discovered here are only applicable under down-front wind and  
264 destabilizing conditions. According to our evaluation, the conditions are met about 31% and 21%  
265 of the time in winter and summer, respectively. It means GSP contributes ~40% in a third of the  
266 winter. This is the most conservative estimation since even in up-front wind conditions GSP is  
267 expected to have a vertical structure similar to AGSP<sup>20,29</sup> and a comparable magnitude of the  
268 GSP contribution to the down-front case will be derived. Meanwhile, the TKE model is a linear  
269 superposition of different kinds of turbulence and their interactions are not considered. For strong  
270 baroclinic fronts, VBP turbulence is inhibited and the surface buoyancy flux tends to characterize  
271 GSP turbulence<sup>18</sup>. Likewise, frontal processes, such as mixed layer instability, tend to restratify  
272 the OSBL and generate positive VBP, also reducing the VBP dominance<sup>30,31</sup>. The full range of  
273 these types of interactions between turbulence energy sources is not yet known, however  
274 additional work on this topic will help further refine future estimates of the global sources of OSBL  
275 turbulence.

276  
277 It is noteworthy that the relative contributions of the turbulence sources vary with depth within the  
278 OSBL, as the vertical decreasing rates of their intensities are different. The relative contribution at  
279 the OSBL mid-depth revealed in this work suggests a significant role of GSP turbulence to the  
280 exchanges between the OSBL and the ocean interior. However, its contribution is not  
281 represented in most regional and climate ocean models, which may be hypothesized to be one of  
282 the key reasons leading to simulated biases of the OSBL. Due to the small frontal arrest scale,  
283 parameterizing GSP turbulence, as would be natural in a model with strict kinetic energy  
284 conservation<sup>32</sup>, offers an alternative future approach to include its contribution in ocean models.

285

## 286 **Methods**

287

### 288 **Model data**

289 Oceanic data including velocity, temperature, and salinity are from a submesoscale-permitting  
290 global model, LLC4320. LLC4320 was simulated by the Massachusetts Institute of Technology  
291 general circulation model (MITgcm) on a Latitude-Longitude polar Cap (LLC) grid<sup>33,34</sup>. The model  
292 has a spatial resolution of 1/48° and 90 vertical layers. The model was initialized successively  
293 from a set of simulations with resolutions of 1/6°, 1/12°, and 1/24°. The K-Profile Parameterization  
294 scheme (KPP) was applied in the simulation. The atmospheric forcing to drive the simulation was  
295 from the European Centre for Medium Range Weather Forecasting (ECMWF) with resolutions of  
296 6 hours in time and 0.14° in space. Tidal forcing was also included in the simulation. LLC4320  
297 was run for 14 months of simulation time, from September 2011 to November 2012, and essential  
298 state variables were stored at hourly snapshots. The model result has been validated against in  
299 situ observations<sup>34,35</sup> and has been widely used for the analysis of submesoscale seasonality,  
300 energy cascade and air-sea flux<sup>22,25,36</sup>. The ECMWF surface fluxes are applied to evaluate  
301 OSBL turbulence. For consistency, we directly use the outputted sea surface fluxes from the  
302 simulation, except for the Stokes drift—from ECMWF ERA5 which has a spatial resolution of 0.5°.  
303 In this work, data in February and August are chosen for analysis. All results shown in this work  
304 are subsampled with a grid spacing of 4°.

305

306 Before the LLC4320 data are used for further analysis, the performance of LLC4320 in  
307 reproducing OSBL fronts needs to be assessed. However, a direct assessment of the buoyancy  
308 gradients is impossible since high resolution global observations are not available. Considering  
309 satellite-derived sea surface temperature (SST) usually have high spatial resolution around 1 km,  
310 a quantitative comparison of SST between LLC4320 and Visible Infrared Imaging Radiometer  
311 Suite (VIIRS) L2 products (with spatial resolutions from 0.75 km at nadir to 1.5 km at the swath  
312 edge) is conducted. Here, SST from LLC4320 is the uppermost 0.5-m layer of the simulation.  
313 Recently, LLC4320 is demonstrated to reproduce the observed distribution of SST patterns well  
314 both globally and regionally<sup>37</sup>. Nevertheless, as OSBL fronts are focused in this work, the spatial  
315 SST variance is assessed using the first-order structure function<sup>38</sup>. As the VIIRS L2 data have

316 missing values due to clouds, the structure function can avoid the effect of these missing values  
 317 and statistically demonstrates the capability of the LLC4320 model in reproducing SST variances.

318  
 319 The first-order structure function here is defined as the difference of SST between the pair of  
 320 points,  $\vec{x}$ , and  $\vec{x} + \vec{r}$ , namely,

$$321 \quad \delta = SST(\vec{x} + \vec{r}) - SST(\vec{x}) \quad (1)$$

322 Then the probability density functions (PDFs) of SST structure function  $\delta$  at different scales ( $r =$   
 323 100 km, 80 km, 60 km, 50km, 40 km, 30 km, 20 km, 10km and 5 km) are calculated based on  
 324 VIIRS and LLC4320 data in the same period (February and August of 2012). To avoid the effect  
 325 of the missing values in VIIRS, we interpolate the LLC4320 data onto the VIIRS grids at the  
 326 corresponding dates, and then avoid the corresponding missing-value regions. Due to the spatial  
 327 resolution limitation, the structure function probabilities of large separations  $r$  from LLC4320 are  
 328 expected to be consistent with VIIRS. But as  $r$  decreases below the effective resolution, the PDFs  
 329 from LLC4320 are speculated to underestimate the SST frontal magnitude from VIIRS. The  
 330 calculated PDF differences between these two datasets in different regions confirm the  
 331 speculation (Fig. S6). The negligible differences between LLC4320 and VIIRS on separation  
 332 scales larger than the effective resolution indicate that LLC4320 reproduces observed SST jumps  
 333 well. However, as the scale decreases below the effective resolution, the underprediction of SST  
 334 jumps begins to become more and more consequential. The positive bias in probability at small  
 335 SST jump magnitude and negative bias in probability at large SST jump magnitude imply that at  
 336 small spatial scale LLC4320 overpredicts small SST jumps and underpredicts large SST jumps  
 337 compared to the real ocean. So, this misestimation is corrected on the buoyancy gradients (see  
 338 the method below).

### 339 340 **Non-dimensional turbulent kinetic energy budget**

341 The TKE budget in the OSBL can be expressed as follows:

$$342 \quad \frac{\partial \bar{e}}{\partial t} = -\overline{\mathbf{u}'\mathbf{w}'} \frac{\partial \overline{u_s'}}{\partial z} - \overline{\mathbf{u}'\mathbf{w}'} \frac{\partial \overline{u_g'}}{\partial z} - \overline{\mathbf{u}'\mathbf{w}'} \frac{\partial \overline{u_a'}}{\partial z} + \overline{w'b'} - \epsilon + F_e. \quad (2)$$

343 Here, the overbars and primes denote time averages and perturbations.  $e = \frac{1}{2}(\mathbf{u}'^2 + \mathbf{w}'^2)$  is the  
 344 TKE. The horizontal velocity is decomposed into three components, the Stokes drift component,  
 345  $\mathbf{u}_s$ , the geostrophic component,  $\mathbf{u}_g$ , and the ageostrophic component,  $\mathbf{u}_a$ , each of which has an  
 346 associated vertical shear production term. These production terms are denoted LSP, GSP, and  
 347 AGSP, respectively. The fourth term on the right-hand side of (1) is the vertical buoyancy  
 348 production (VBP) which generates TKE when the ocean surface loses buoyancy through surface  
 349 cooling or salt fluxes. The fifth term is the molecular dissipation of TKE. The last term is the  
 350 vertical TKE transport. Assuming a steady state and a negligible  $F_e$ , an equilibrium is reached  
 351 between the TKE dissipation and the TKE sources,

$$352 \quad \epsilon = -\overline{\mathbf{u}'\mathbf{w}'} \frac{\partial \overline{u_s'}}{\partial z} - \overline{\mathbf{u}'\mathbf{w}'} \frac{\partial \overline{u_g'}}{\partial z} - \overline{\mathbf{u}'\mathbf{w}'} \frac{\partial \overline{u_a'}}{\partial z} + \overline{w'b'}. \quad (3)$$

353 This equation can be simplified into a non-dimensional expression for the TKE budget under  
 354 destabilizing surface buoyancy forcing at the mid-depth of the OSBL,

$$355 \quad \frac{\epsilon(z=0.5h)}{u_*^3/h} = A_L La_t^{-2} + A_G \frac{h}{L_S} + A_S + A_C La_t^{-2} \frac{h}{L_L}, \quad (4)$$

356 where  $h$  is the OSBL thickness as determined by using an offline KPP scheme,  $u_* = \sqrt{\frac{|\tau_w|}{\rho}}$  is the  
 357 friction velocity ( $\tau_w$  is the sea surface wind stress,  $\rho$  is the seawater density),  $La_t = \sqrt{\frac{u_*}{u_s}}$  is the  
 358 turbulent Langmuir number<sup>39</sup>. The effect of misalignments between Stokes drift, wind direction  
 359 and Langmuir cells is considered in the calculation<sup>40</sup>.  $L_S = \frac{u_* f}{M^2 \cos \theta}$  is the geostrophic shear stability  
 360 length ( $f$  is the Coriolis parameter,  $M^2 = |\nabla_h b|$  is the horizontal buoyancy gradient magnitude,  $\theta$   
 361 is the angle between the wind and the frontal geostrophic shear vectors)<sup>20</sup>,  $L_L = \frac{u_*^2 u_s}{B_0}$  is the  
 362 Langmuir stability length ( $B_0$  is the sea surface buoyancy flux)<sup>10</sup>. Other parameters are taken as  
 363 the following values:  $A_L = 0.22$ ,  $A_G = 0.5$ ,  $A_S = 2[1 - \exp(-0.5La_t)]$ ,  $A_C = 0.3$ . The equation

364 extends the TKE budget equation of Belcher et al. <sup>10</sup> by including the GSP term. Here, the  
365 parameter  $A_G=0.5$  in the GSP term is determined by the vertical structure of GSP under forced  
366 symmetric instability at fronts <sup>41</sup>. Here, the budget equation is only applicable for fronts with down-  
367 front winds and GSP is potentially underestimated, as it has been reported elsewhere<sup>16</sup> that VBP  
368 tends to interact with GSP and strengthen GSP under destabilizing conditions and this interaction  
369 is neglected. Nevertheless, further comparison with the OSMOSIS observations demonstrates  
370 the robustness of the TKE model under surface buoyancy loss which can statistically reproduce  
371 OSBL dissipation (see section below).

372

373 The directly calculated horizontal buoyancy gradient  $M^2$  heavily depends on the spatial  
374 resolution. To eliminate this dependence, the calculated  $M^2$  is rescaled according to its spectral  
375 characteristic by assuming OSBL fronts are arrested under TTW balance (see sections below).  
376 Because OSBL fronts are not always arrested (such as during frontogenesis and frontolysis), the  
377 estimation of the submesoscale turbulence here is a maximum magnitude that OSBL fronts can  
378 reach, not an average over their whole life. This does not qualitatively alter our results is  
379 confirmed above by analysis of the raw model buoyancy gradients, which likewise indicate a  
380 leading role for GSP in OSBL turbulence.

381

### 382 **Validation of the TKE model**

383 To further validate the TKE production model the analysis is applied to in situ observations from  
384 the OSMOSIS project <sup>17, 42</sup> (estimating  $\frac{u_*^3}{h}$ ,  $La_t$ ,  $\frac{h}{L_L}$ , and  $\frac{h}{L_S}$ ) and the results are compared to the  
385 directly observed dissipation rate. As a part of the OSMOSIS project, nine moorings were  
386 deployed in the northeast Atlantic Ocean for the period September 2012–September 2013. With a  
387 centrally located mooring, the remaining moorings consisted of two quadrilaterals. It is a  
388 13km×13km outer box consisting of four moorings, while it is a 2.5km×2.5km inner one  
389 consisting of the remaining four. The resolution of the inner mooring is tended to resolve  
390 submesoscale fronts <sup>17, 42</sup>. The moorings were equipped with Conductivity–Temperature–Depth  
391 (CTD) instruments spanning a depth range of 30–530 m with a sampling rate of 5 min. In this  
392 work, temperature and salinity observed at the central and inner moorings are used for analysis.  
393 Temperature and salinity are interpolated vertically into 10-m bins in the range of 50–300 m. In  
394 addition to the mooring array, seagliders were also deployed during the OSMOSIS project, and  
395 dissipation rates in the upper ocean were derived from the glider observations <sup>43</sup>.

396

397 In the TKE model, the quantities to be determined are calculated as follows. The OSBL thickness  
398  $h$  is determined as the depth where the observed dissipation rate decreases to a threshold value  
399 of  $1 \times 10^{-8} \text{ W kg}^{-1}$ . Then, the dissipation rate at the OSBL mid depth is obtained. The frictional  
400 and the convective velocities,  $u_*$  and  $w_*$  are calculated based on the atmospheric momentum and  
401 buoyancy fluxes provided by the ECMWF ERA5 with a spatial resolution of  $0.25^\circ$ . The Stokes drift  
402  $u_s$ , and other wave parameters, are provided from the ECMWF ERA5 with a spatial resolution of  
403  $0.5^\circ$ . The buoyancy gradient  $M^2$  is calculated using the observations of the central and inner  
404 moorings. As the inner moorings can only partially resolve submesoscale fronts, we also correct  
405 the buoyancy gradient using the rescaling method with the amplification factor derived from the  
406 LLC4320. The mooring observations are confined below 50 m, hence the validation is conducted  
407 in winter (January 2013–April 2013) during which the ocean has a deep OSBL thickness in  
408 excess of 100 m. All data are interpolated to the times of the glider observations. Furthermore,  
409 compared to  $C_L = 0.25$ , (derived from turbulence resolving numerical simulations), we decide to  
410 use  $C_L = 1$  in the frontal arrest scale equation which is found to reproduce a better result (**Fig.**  
411 **S7**).

412

413 The expectation is that the produced energy will balance the dissipation of energy, although the  
414 transport of energy by the oceanic flow can locally violate this balance. The time series of the  
415 dissipation rate at the OSBL mid-depth exhibits dramatic intermittency with variation across

416 several orders of magnitude (**Fig. S7a**). When observed dissipation is compared with the  
 417 summed combination of LSP, VBP and AGSP, the sum is typically too small. Including the  
 418 dissipation from a four-source sum, with the GSP, better reproduces the high-dissipation events  
 419 (although it also predicts too few weak dissipation events). PDFs of the dissipation demonstrate  
 420 the capability of the TKE production model more explicitly (**Fig. S7b**). The production without  
 421 GSP tends to underestimate the observed dissipation—that is a sink stronger than the sources.  
 422 By contrast, high GSP events shift the PDF towards larger values, correcting the underestimation.  
 423 Notably, the corrected PDF peak is more consistent with observations.

424  
 425 A further comparison between the dissipation rates estimated using glider observations and  
 426 estimates from the LLC4320 simulation is conducted to assess if the buoyancy gradient  
 427 correction is justified (**Fig. S7c**). As there is no overlap between the OSMOSIS winter observation  
 428 period (January 2012–April 2012) and the winter simulated with LLC4320 (here January 2012–  
 429 April 2012), the non-dimensional values scaled by the simultaneously observed/modeled  $u_*^3/h$   
 430 are compared. The production from LLC4320 shows a general similarity to the OSMOSIS  
 431 production, both when GSP is included and excluded—so long as the LLC4320 GSP is corrected  
 432 for limited model resolution (**Fig. S7c**). Using only the uncorrected GSP for LLC4320 (i.e.,  
 433 calculated based on the original buoyancy gradients from the LLC4320 without rescaling)  
 434 underestimates the observed dissipation. The result here is quite different from Buckingham et al.  
 435 <sup>42</sup>, who reported a less important contribution of GSP to OSBL dissipation. In addition to the  
 436 buoyancy gradient correction—which adjusts for limitations in the horizontal resolution of the  
 437 mooring array (**Fig. S8**)—another key difference that should be noted is the depth investigated. A  
 438 fixed depth of 45 m is used in Buckingham et al.<sup>42</sup>, which is much shallower in winter compared to  
 439 the mid-depth of the mixed layer used here. LSP turbulence tends to concentrate near the  
 440 surface and decreases more sharply with depth compared to GSP turbulence. Our work suggests  
 441 an increasing relative significance of GSP turbulence away from the surface.

#### 442 443 **Buoyancy gradient rescaling**

444 The buoyancy gradient from the LLC4320 is rescaled to account for the effect of horizontal  
 445 resolution in the numerical model following the method in Fox-Kemper et al.<sup>28</sup>. The power  
 446 spectrum of the buoyancy averaged over the OSBL tends to decay with a constant slope (usually  
 447 around  $k^{-2}$ ). Thus, the spectrum of the horizontal buoyancy gradient averaged in the OSBL tends  
 448 to be flat or white, i.e.,  $\sim k^0$ . Assuming an isotropic, power-law behavior with a spectral slope of  $k^a$   
 449 for the buoyancy gradient, the integral of the buoyancy gradient over an integrated domain  $L_b$   
 450 range down to the effective model resolution  $L_{eff}$  can be related to the wavenumber spectrum  
 451  $B_0 k^a$ ,

$$452 \quad \int_{L_{eff}}^{L_b} \int_0^{2\pi} |\langle \nabla_H b \rangle|^2 r dr d\theta = \int_{\frac{2\pi}{L_b}}^{\frac{2\pi}{L_{eff}}} B_0 k^a dk. \quad (5)$$

453 Similarly, the integral from the basin scale down to the frontal scale  $L_f$  is

$$454 \quad \int_{L_f}^{L_b} \int_0^{2\pi} |\langle \nabla_H b \rangle|^2 r dr d\theta = \int_{\frac{2\pi}{L_b}}^{\frac{2\pi}{L_f}} B_0 k^a dk. \quad (6)$$

455 Combing these two equations yields an estimate for the degree of underestimation of the  
 456 modeled buoyancy gradient magnitude relative to that at the frontal scale,

$$457 \quad \frac{\int_{L_{eff}}^{L_b} \int_0^{2\pi} |\nabla_H b|^2 r dr d\theta}{\int_{L_f}^{L_b} \int_0^{2\pi} |\nabla_H b|^2 r dr d\theta} = \frac{\int_{\frac{2\pi}{L_b}}^{\frac{2\pi}{L_{eff}}} B_0 k^a dk}{\int_{\frac{2\pi}{L_b}}^{\frac{2\pi}{L_f}} B_0 k^a dk} = \left( \frac{L_f}{L_{eff}} \right)^{1+a} \frac{1^{1+a} - \frac{L_{eff}^{1+a}}{L_b^{1+a}}}{1^{1+a} - \frac{L_f^{1+a}}{L_b^{1+a}}} \approx \left( \frac{L_f}{L_{eff}} \right)^{1+a}. \quad (7)$$

458 If  $a=0$ , the equation scales as estimated in Fox-Kemper et al.<sup>28</sup> ("no-slope corrected"). However,  
 459 according to our evaluation based on the LCC4320 result, the spectra in zonal and meridional at  
 460 different regions generally have slightly negative slopes, rather than zero slopes (**Fig. S9**).

461 Estimates of the slope are therefore derived by linearly fitting over the range determined by the

462 domain size and the effective resolution  $L_{eff} = 7\Delta s$  (this resolution corresponds roughly to the  
 463 maximum resolved wavenumber before the spectra roll off sharply due to numerical dissipation)  
 464 <sup>34</sup>. Based on the slopes over the globe, the original buoyancy gradient magnitude derived directly  
 465 from LCC4320 (“uncorrected”) is rescaled based on the estimated true frontal width (“corrected”)  
 466 by,

$$467 \quad \nabla_H b_f = \left(\frac{L_{eff}}{L_f}\right)^{\frac{1+a}{2}} \nabla_H b_{\Delta s}. \quad (8)$$

468 It should be noted that the amplification factor  $\left(\frac{L_{eff}}{L_f}\right)^{\frac{1+a}{2}}$  is directly taken as 1 at low latitudes when

469  $L_{eff} < L_f$ , i.e., where fronts are resolved. As shown in **Fig. S10**, the amplification factor  $\left(\frac{L_{eff}}{L_f}\right)^{\frac{1+a}{2}}$   
 470 exceeds 6 at mid latitudes.  
 471

### 472 **Calculation of frontal arrest scale**

473 Geostrophic adjustment theory predicts that the width of a front tends to follow the local  
 474 deformation radius <sup>44</sup>. But in the OSBL, strong turbulence breaks the geostrophic balance, and  
 475 near-surface fronts are sharpened by strain-induced and surface-induced frontogenesis until they  
 476 are arrested at a smaller scale by surface-forced turbulence, typically on a scale where TTW  
 477 balance holds <sup>12, 45, 46, 47</sup>. Thus, the front width under TTW is believed to be the scale where the  
 478 fronts in the OSBL are arrested and persistent. For the TTW balance,

$$479 \quad \nabla_H b = -f\mathbf{k} \times \frac{\partial \bar{u}}{\partial z} + \frac{\partial^2}{\partial z^2} (\mathbf{u}'w'), \quad (9)$$

480 the Reynolds stress term can be parameterized as  $\mathbf{u}'w' = (m_* u_*^3 + n_* w_*^3)^{2/3}$  from the planetary  
 481 boundary layer scheme (ePBL; Reichl and Hallberg, 2018). Thus, a scaling method for the  
 482 arrested frontal width is proposed by Bodner et al. <sup>21</sup>,

$$483 \quad L_f = C_L \frac{(m_* u_*^3 + n_* w_*^3)^{2/3}}{f^2 h}. \quad (10)$$

484 Here, only destabilizing surface buoyancy forcing that produces TKE is considered. Under the  
 485 destabilizing condition, the mechanical coefficient  $m_*$  measures the efficiency of the mechanical  
 486 forcing in changing OSBL TKE and is scaled by combining Equations (29) and (36) of Reichl and  
 487 Hallberg <sup>48</sup>, while the convection coefficient  $n_* = 0.066$  measures the efficiency of the buoyancy  
 488 forcing in changing OSBL TKE and is taken as a constant.  $w_* = (B_0 h)^{1/3}$  is the convective  
 489 velocity.  $f$  is the Coriolis parameter,  $h$  is the OSBL thickness, and  $C_L$  is a constant parameter. In  
 490 this work, we decide to use a more conservative value of  $C_L = 1$  based on a comparison with  
 491 observations (Text S1) instead of  $C_L = 0.25$  suggested by Bodner et al. <sup>21</sup> based on a limited  
 492 number of Large Eddy Simulations. Details are referred to Bodner et al. <sup>21</sup>.

493 The frontal width is calculated based on the LCC4320 outputs. We evaluate the robustness of  
 494 that dataset using a simulation of upper ocean mixing without feedback using the General Ocean  
 495 Turbulence Model (GOTM). GOTM is a one-dimensional water column model that is focused on  
 496 ocean turbulence <sup>49</sup>. The version of GOTM used here is compiled with the ePBL closure <sup>11, 48</sup>. On  
 497 each grid point of the subsampled 4° LLC4320 grids, GOTM simulation is conducted for two  
 498 months, February and August. The initial and boundary conditions are provided by LLC4320. For  
 499 consistency, we also directly use the outputted sea surface fluxes from the simulation, which are  
 500 provided by the ECMWF dataset. The vertical spacings of the simulations are as fine as  
 501 centimeters, which ensures the capability of the GOTM in reproducing the OSBL. As Bodner et al.  
 502 <sup>21</sup> proposed the frontal arrest scale based on the ePBL, we apply the ePBL scheme in the GOTM  
 503 simulations. Hence, the frontal scale calculated from the GOTM outputs tends to be more  
 504 dynamically consistent. By comparing the frontal scales between the GOTM and LLC4320, we  
 505 can estimate the sensitivity of the frontal width to the sub-grid turbulence closures (**Fig. S11**). The  
 506 frontal width over the globe varies across several orders of magnitude with latitude, from  
 507 hundreds of meters to tens of kilometers. The frontal width is larger in summer than in winter.  
 508 Despite using different sub-grid turbulence schemes (KPP in LLC4320 and ePBL in GOTM), the

509 calculated frontal widths resemble each other which demonstrates that the frontal scale  
510 calculated here is insensitive to the turbulence closures. Finally, while the GSP and horizontal  
511 shear production of the fronts themselves should contribute somewhat to the turbulence causing  
512 the arrest, the robustness of the frontal width estimates to various TKE energy sources indicates  
513 these effects are unlikely to change the result significantly. These results indicates that the  
514 calculated frontal width is not sensitive to the details of the model and its chosen sub-grid  
515 turbulence closure.

516  
517

### 518 **Acknowledgments**

519 The authors wish to thank the Estimating the Circulation and Climate of the Oceans (ECCO) team  
520 (<https://ecco.jpl.nasa.gov>) and NASA High-End Computing (HEC) from the NASA Advanced  
521 Superconducting (NAS) Division at the Ames Research Center for the LLC4320 simulation data.  
522 This work is supported by the National Natural Science Foundation of China (42176023). J.W.  
523 was supported by the National Science Foundation under grant OCE-2148945. B.F-K. was  
524 supported by NSF OCE-2148945 and NOAA NA19OAR4310366.

525

### 526 **Data availability**

527 The LLC4320 data can be directly accessed from the ECCO Data Portal  
528 (<https://data.nas.nasa.gov/ecco/data.php>), or conveniently downloaded using the xmitgcm  
529 package (<https://xmitgcm.readthedocs.io/en/latest/index.html>). The Stokes drift of the ECMWF  
530 ERA5 is accessible at the Copernicus Climate Change Service (C3S) Climate Data Store  
531 (<https://cds.climate.copernicus.eu/cdsapp#!/dataset/reanalysis-era5-single-levels?tab=form>). The  
532 OSMOSIS data is available at the British Oceanographic Data Centre after registration  
533 ([https://www.bodc.ac.uk/data/bodc\\_database/nodb/search/](https://www.bodc.ac.uk/data/bodc_database/nodb/search/)). The VIIRS L2 SST product is  
534 available at the JPL Physical Oceanography Distributed Active Archive Center  
535 (<https://doi.org/10.5067/GHVRS-2PO28>)

536

### 537 **Author contributions**

538 J.D., B.F. and J.W. conceived the experiments, analyzed the results and wrote the manuscript.  
539 A.B. and H.Z. helped with the analysis of the numerical simulations. Y.X. helped with the analysis  
540 of the observations. J.D., B.F., J.W., A.B. and C.D. reviewed the manuscript.

541

### 542 **Competing interests**

543 The authors declare no competing interests.

544

### 545 **Additional information**

546 Supplementary information is available for this paper at .

547

548

549



550 **References**

- 551 1. Fox-Kemper B, Johnson L, Qiao F. Chapter 4 - Ocean near-surface layers. In: Meredith M,  
552 Naveira Garabato A (eds). *Ocean Mixing*. Elsevier, 2022, pp 65-94.  
553
- 554 2. McCartney MS. Subantarctic mode water. *Woods Hole Oceanographic Institution*  
555 *Contribution* 1979, **3773**: 103-119.  
556
- 557 3. Sallée JB, Shuckburgh E, Bruneau N, Meijers AJ, Bracegirdle TJ, Wang Z. Assessment of  
558 Southern Ocean mixed-layer depths in CMIP5 models: Historical bias and forcing  
559 response. *Journal of Geophysical Research: Oceans* 2013, **118**(4): 1845-1862.  
560
- 561 4. Thomas MD, Tréguier A-M, Blanke B, Deshayes J, Voldoire A. A Lagrangian method to  
562 isolate the impacts of mixed layer subduction on the meridional overturning circulation in  
563 a numerical model. *Journal of Climate* 2015, **28**(19): 7503-7517.  
564
- 565 5. Frankignoul C, Hasselmann K. Stochastic climate models, Part II Application to sea-surface  
566 temperature anomalies and thermocline variability. *Tellus* 1977, **29**(4): 289-305.  
567
- 568 6. Price JF, Weller RA, Pinkel R. Diurnal cycling: Observations and models of the upper ocean  
569 response to diurnal heating, cooling, and wind mixing. *Journal of Geophysical Research:*  
570 *Oceans* 1986, **91**(C7): 8411-8427.  
571
- 572 7. Klein P, Coste B. Effects of wind-stress variability on nutrient transport into the mixed layer.  
573 *Deep Sea Research Part A Oceanographic Research Papers* 1984, **31**(1): 21-37.  
574
- 575 8. Rodgers KB, Aumont O, Mikaloff Fletcher S, Plancherel Y, Bopp L, de Boyer Montégut C, *et*  
576 *al.* Strong sensitivity of Southern Ocean carbon uptake and nutrient cycling to wind stirring.  
577 *Biogeosciences* 2014, **11**(15): 4077-4098.  
578
- 579 9. Large WG, McWilliams JC, Doney SC. Oceanic vertical mixing: A review and a model with  
580 a nonlocal boundary layer parameterization. *Reviews of geophysics* 1994, **32**(4): 363-403.  
581
- 582 10. Belcher SE, Grant AL, Hanley KE, Fox-Kemper B, Van Roekel L, Sullivan PP, *et al.* A global  
583 perspective on Langmuir turbulence in the ocean surface boundary layer. *Geophysical*  
584 *Research Letters* 2012, **39**(18).  
585
- 586 11. Li Q, Reichl BG, Fox-Kemper B, Adcroft AJ, Belcher SE, Danabasoglu G, *et al.* Comparing  
587 ocean surface boundary vertical mixing schemes including Langmuir turbulence. *Journal*  
588 *of Advances in Modeling Earth Systems* 2019, **11**(11): 3545-3592.  
589
- 590 12. Sullivan PP, McWilliams JC. Frontogenesis and frontal arrest of a dense filament in the  
591 oceanic surface boundary layer. *Journal of Fluid Mechanics* 2018, **837**: 341-380.  
592
- 593 13. Zheng Z, Harcourt RR, D'Asaro EA. Evaluating Monin–Obukhov Scaling in the Unstable  
594 Oceanic Surface Layer. *Journal of Physical Oceanography* 2021, **51**(3): 911-930.

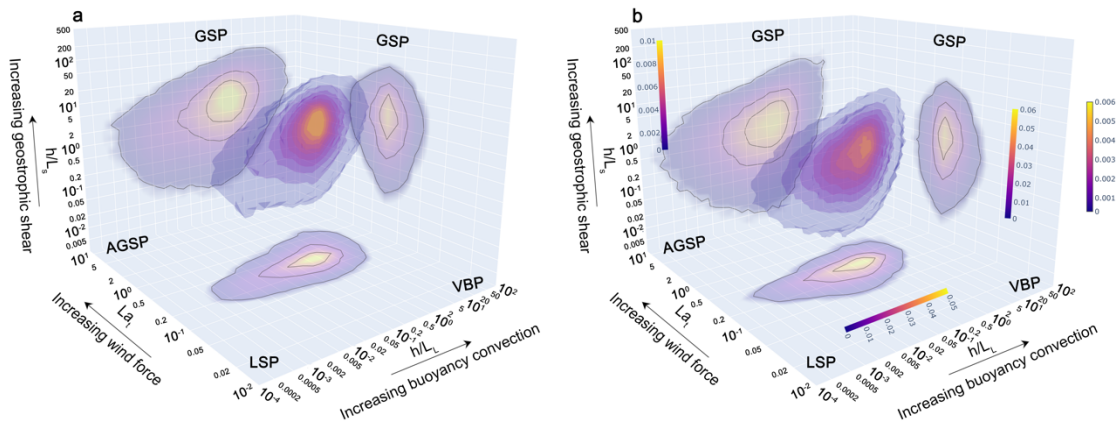
- 595  
596 14. Ferris L, Gong D, Clayson CA, Merrifield S, Shroyer EL, Smith M, *et al.* Shear turbulence in  
597 the high-wind Southern Ocean using direct measurements. *Journal of Physical*  
598 *Oceanography* 2022, **52**(10): 2325-2341.  
599
- 600 15. D'asaro E, Lee C, Rainville L, Harcourt R, Thomas L. Enhanced turbulence and energy  
601 dissipation at ocean fronts. *science* 2011, **332**(6027): 318-322.  
602
- 603 16. Thomas LN, Taylor JR, Ferrari R, Joyce TM. Symmetric instability in the Gulf Stream. *Deep*  
604 *Sea Research Part II: Topical Studies in Oceanography* 2013, **91**: 96-110.  
605
- 606 17. Yu X, Naveira Garabato AC, Martin AP, Gwyn Evans D, Su Z. Wind-forced symmetric  
607 instability at a transient mid-ocean front. *Geophysical Research Letters* 2019, **46**(20):  
608 11281-11291.  
609
- 610 18. Bachman SD, Fox-Kemper B, Taylor JR, Thomas LN. Parameterization of frontal symmetric  
611 instabilities. I: Theory for resolved fronts. *Ocean Modelling* 2017, **109**: 72-95.  
612
- 613 19. Wenegrat JO, Thomas LN, Sundermeyer MA, Taylor JR, D'Asaro EA, Klymak JM, *et al.*  
614 Enhanced mixing across the gyre boundary at the Gulf Stream front. *Proceedings of the*  
615 *National Academy of Sciences* 2020, **117**(30): 17607-17614.  
616
- 617 20. Skillingstad ED, Duncombe J, Samelson RM. Baroclinic frontal instabilities and turbulent  
618 mixing in the surface boundary layer. Part II: Forced simulations. *Journal of Physical*  
619 *Oceanography* 2017, **47**(10): 2429-2454.  
620
- 621 21. Bodner AS, Fox-Kemper B, Johnson L, Van Roekel LP, McWilliams JC, Sullivan PP, *et al.*  
622 Modifying the Mixed Layer Eddy Parameterization to Include Frontogenesis Arrest by  
623 Boundary Layer Turbulence. *Journal of Physical Oceanography* 2022.  
624
- 625 22. Su Z, Wang J, Klein P, Thompson AF, Menemenlis D. Ocean submesoscales as a key  
626 component of the global heat budget. *Nature communications* 2018, **9**(1): 1-8.  
627
- 628 23. Cael BB, Mashayek A. Log-Skew-Normality of Ocean Turbulence. *Physical Review Letters*  
629 2021, **126**(22): 224502.  
630
- 631 24. Pearson B, Fox-Kemper B. Log-normal turbulence dissipation in global ocean models.  
632 *Physical review letters* 2018, **120**(9): 094501.  
633
- 634 25. Dong J, Fox-Kemper B, Zhang H, Dong C. The seasonality of submesoscale energy  
635 production, content, and cascade. *Geophysical Research Letters* 2020, **47**(6):  
636 e2020GL087388.  
637
- 638 26. Callies J, Ferrari R, Klymak JM, Gula J. Seasonality in submesoscale turbulence. *Nature*  
639 *Communications* 2015, **6**(1): 6862.  
640

- 641 27. Dong J, Fox-Kemper B, Zhang H, Dong C. The scale of submesoscale baroclinic instability  
642 globally. *Journal of Physical Oceanography* 2020, **50**(9): 2649-2667.  
643
- 644 28. Fox-Kemper B, Danabasoglu G, Ferrari R, Griffies S, Hallberg R, Holland M, *et al.*  
645 Parameterization of mixed layer eddies. III: Implementation and impact in global ocean  
646 climate simulations. *Ocean Modelling* 2011, **39**(1-2): 61-78.  
647
- 648 29. Moeng C-H, Sullivan PP. A comparison of shear-and buoyancy-driven planetary boundary  
649 layer flows. *Journal of Atmospheric Sciences* 1994, **51**(7): 999-1022.  
650
- 651 30. Mahadevan A, D'asaro E, Lee C, Perry MJ. Eddy-driven stratification initiates North Atlantic  
652 spring phytoplankton blooms. *Science* 2012, **337**(6090): 54-58.  
653
- 654 31. Taylor JR. Turbulent mixing, restratification, and phytoplankton growth at a submesoscale  
655 eddy. *Geophysical Research Letters* 2016, **43**(11): 5784-5792.  
656
- 657 32. Eden C, Czeschel L, Olbers D. Toward Energetically Consistent Ocean Models. *Journal of*  
658 *Physical Oceanography* 2014, **44**(12): 3160-3184.  
659
- 660 33. Menemenlis D, Campin J-M, Heimbach P, Hill C, Lee T, Nguyen A, *et al.* ECCO2: High  
661 resolution global ocean and sea ice data synthesis. *Mercator Ocean Quarterly Newsletter*  
662 2008, **31**(October): 13-21.  
663
- 664 34. Rocha CB, Chereskin TK, Gille ST, Menemenlis D. Mesoscale to submesoscale wavenumber  
665 spectra in Drake Passage. *Journal of Physical Oceanography* 2016, **46**(2): 601-620.  
666
- 667 35. Rocha CB, Gille ST, Chereskin TK, Menemenlis D. Seasonality of submesoscale dynamics in  
668 the Kuroshio Extension. *Geophysical Research Letters* 2016, **43**(21): 11,304-311,311.  
669
- 670 36. Viglione GA, Thompson AF, Flexas MM, Sprintall J, Swart S. Abrupt transitions in  
671 submesoscale structure in Southern Drake Passage: Glider observations and model results.  
672 *Journal of Physical Oceanography* 2018, **48**(9): 2011-2027.  
673
- 674 37. Gallmeier KM, Prochaska JX, Cornillon P, Menemenlis D, Kelm M. An evaluation of the  
675 LLC4320 global ocean simulation based on the submesoscale structure of modeled sea  
676 surface temperature fields. *Geoscientific Model Development Discussions* 2023: 1-42.  
677
- 678 38. Yu K, Dong C, King GP. Turbulent kinetic energy of the ocean winds over the Kuroshio E  
679 xtension from Quik SCAT winds (1999–2009). *Journal of Geophysical Research: Oceans*  
680 2017, **122**(6): 4482-4499.  
681
- 682 39. McWILLIAMS JC, Sullivan PP, Moeng C-H. Langmuir turbulence in the ocean. *Journal of*  
683 *Fluid Mechanics* 1997, **334**: 1-30.  
684
- 685 40. Van Roekel L, Fox-Kemper B, Sullivan P, Hamlington P, Haney S. The form and orientation  
686 of Langmuir cells for misaligned winds and waves. *Journal of Geophysical Research:*

687            *Oceans* 2012, **117**(C5).  
688  
689    41.    Thomas LN, Taylor JR. Reduction of the usable wind-work on the general circulation by  
690            forced symmetric instability. *Geophysical Research Letters* 2010, **37**(18).  
691  
692    42.    Buckingham CE, Lucas NS, Belcher SE, Rippeth TP, Grant AL, Le Sommer J, *et al.* The  
693            contribution of surface and submesoscale processes to turbulence in the open ocean  
694            surface boundary layer. *Journal of Advances in Modeling Earth Systems* 2019, **11**(12):  
695            4066-4094.  
696  
697    43.    Evans DG, Lucas NS, Hemsley V, Frajka-Williams E, Naveira Garabato AC, Martin A, *et al.*  
698            Annual cycle of turbulent dissipation estimated from Seagliders. *Geophysical Research*  
699            *Letters* 2018, **45**(19): 10,560-510,569.  
700  
701    44.    Tandon A, Garrett C. Mixed layer restratification due to a horizontal density gradient.  
702            *Journal of Physical Oceanography* 1994, **24**(6): 1419-1424.  
703  
704    45.    Gula J, Molemaker MJ, McWilliams JC. Submesoscale cold filaments in the Gulf Stream.  
705            *Journal of Physical Oceanography* 2014, **44**(10): 2617-2643.  
706  
707    46.    McWilliams JC, Gula J, Molemaker MJ, Renault L, Shchepetkin AF. Filament frontogenesis  
708            by boundary layer turbulence. *Journal of Physical Oceanography* 2015, **45**(8): 1988-2005.  
709  
710    47.    Wenegrat JO, McPhaden MJ. Wind, waves, and fronts: Frictional effects in a generalized  
711            Ekman model. *Journal of Physical Oceanography* 2016, **46**(2): 371-394.  
712  
713    48.    Reichl BG, Hallberg R. A simplified energetics based planetary boundary layer (ePBL)  
714            approach for ocean climate simulations. *Ocean Modelling* 2018, **132**: 112-129.  
715  
716    49.    Lars Umlauf HBaKB. GOTM: Source code and Test Case Documentation Version 4.0; 2005.  
717  
718  
719

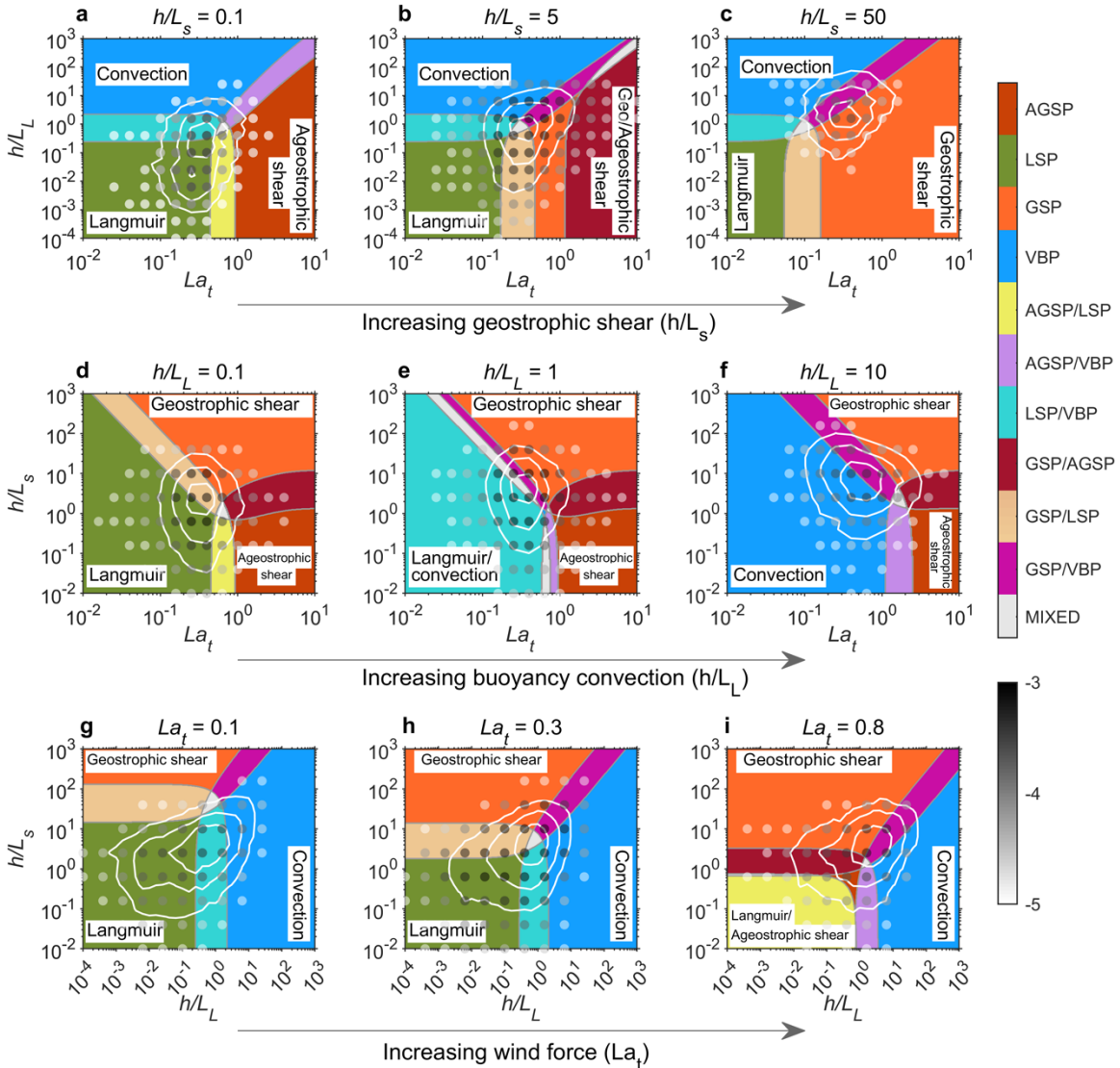
720  
721  
722

## Figures



723  
724  
725  
726  
727  
728  
729  
730  
731  
732  
733

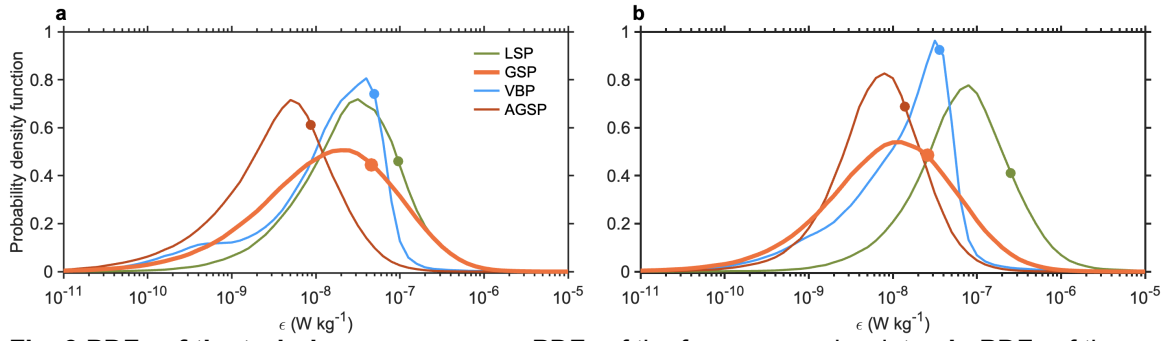
**Fig. 1 Three-dimensional global probability density of the three parameters. a,** The probability density in winter. **b,** The probability density in summer. The three parameters are turbulent Langmuir number  $La_t$  of the x-axis, the ratio of the boundary layer depth to the Langmuir stability length  $h/L_L$  of the y-axis, and the ratio of the boundary layer depth to the geostrophic shear stability length  $h/L_s$  of the z-axis. The two-dimensional projections of the distributions are also shown. The black contours enclose 30%, 60%, and 90% of the global values. Each source of turbulence is labeled and the contribution of fronts (GSP) is highlighted as the geostrophic shear along the z-axis is increased.



735  
 736  
 737  
 738  
 739  
 740  
 741  
 742  
 743  
 744  
 745  
 746  
 747

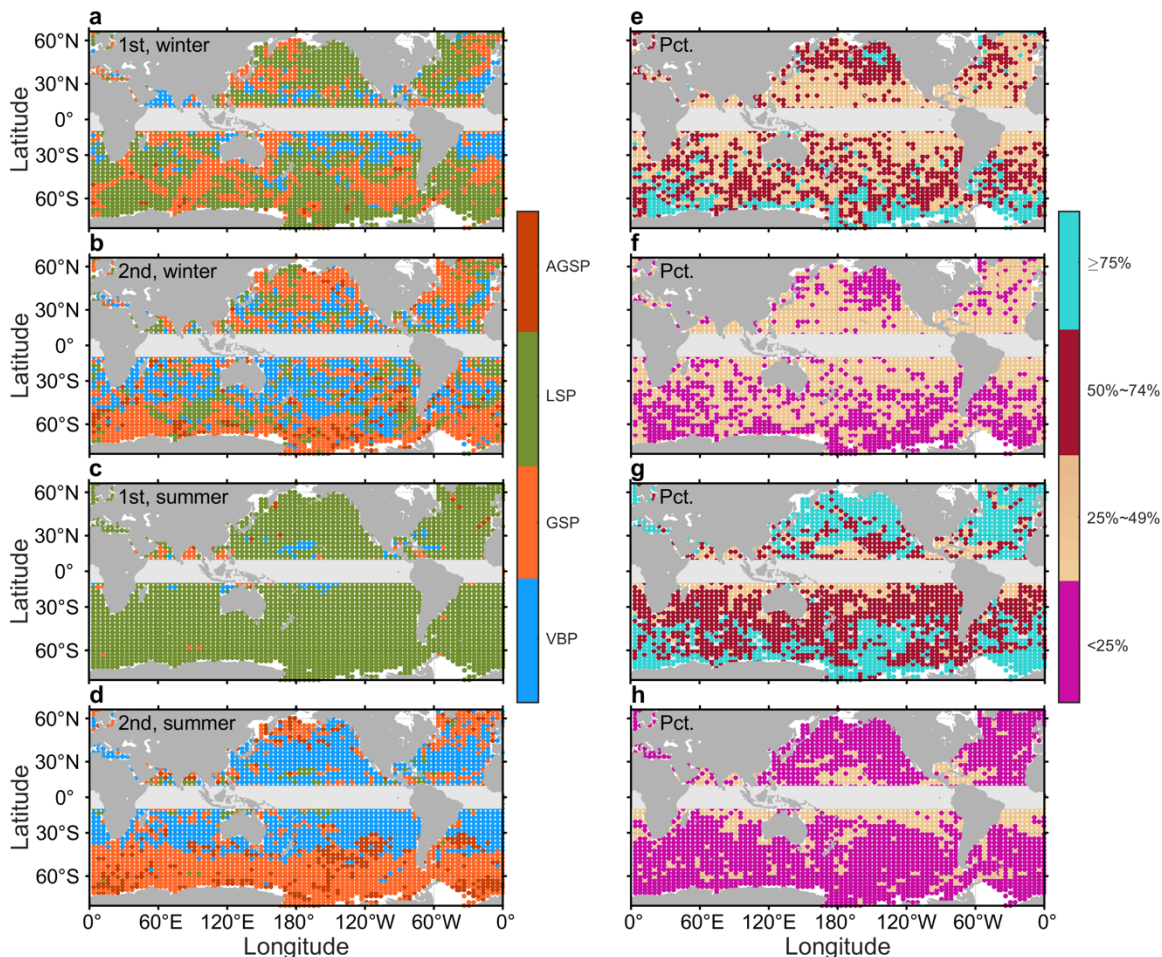
**Fig. 2** Turbulence regimes in parameter slices in winter. **a**,  $h/L_s=0.1$ . **b**,  $h/L_s=5$ . **c**,  $h/L_s=50$ . **d**,  $h/L_L=0.1$ . **e**,  $h/L_L=1$ . **f**,  $h/L_L=10$ . **g**,  $La_t=0.1$ . **h**,  $La_t=0.3$ . **i**,  $La_t=0.8$ . The regimes are defined by the dominant production terms in the TKE budget. The white contours enclose 30%, 60%, and 90% of the locations with the corresponding values. A regime is considered dominant when its dissipation contribution exceeds 75% of the total dissipation, otherwise, it is a two-turbulence-mixed regime when two TKE sources both contribute more than 25% while all others contribute less than 25%, and lastly, it is a mixed regime if more than three sources of turbulence contribute more than 25%<sup>11</sup>. The dots denote the possibility density (in logarithm with 10-base) along these slices from **Fig. 1**. The distributions indicate that GSP is an important regime for OSBL turbulence over the globe, especially at locations with strong frontal geostrophic shears.





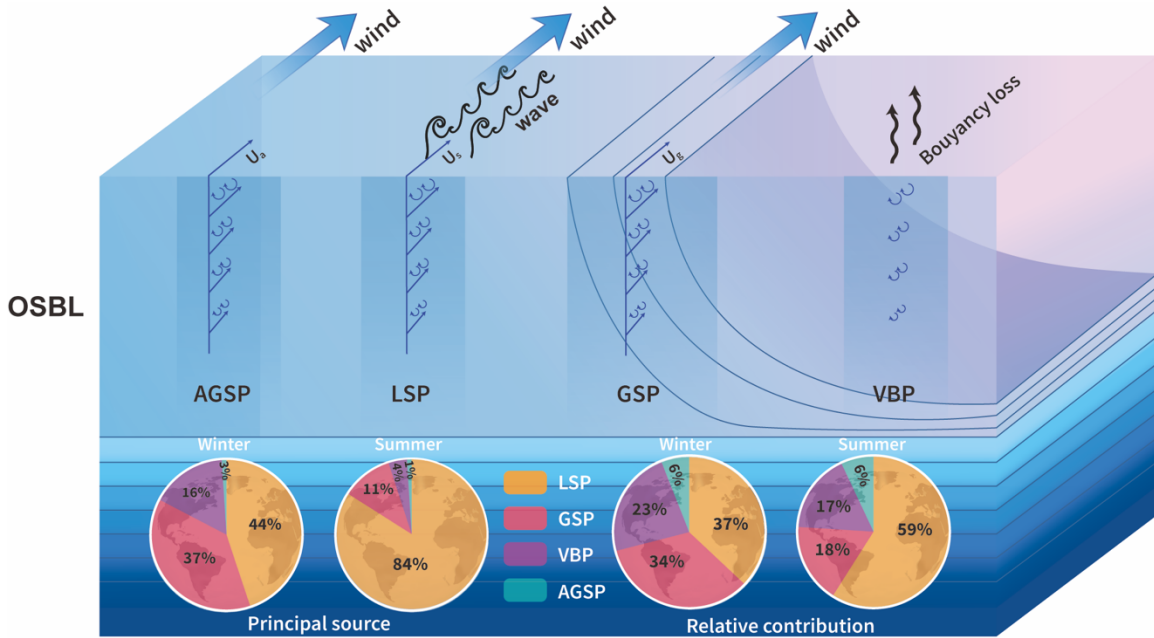
748  
749  
750  
751  
752  
753  
754

**Fig. 3 PDFs of the turbulence sources.** **a**, PDFs of the four sources in winter. **b**, PDFs of the four sources in summer. The dots indicate the corresponding global mean value of each distribution. The log-normal distribution of the PDFs suggests that the mean and integral of OSBL dissipation are determined by intermittent high dissipation rates. The highest intermittency of GSP can also be derived from the distributions.



756  
757  
758  
759  
760  
761  
762  
763  
764  
765

**Fig. 4. Global distributions of the two most likely dominant sources at each location.** **a**, The first most likely dominant sources in winter. **b**, The second most likely dominant sources in winter. **c**, The first most likely dominant sources in summer. **d**, The second most likely dominant sources in summer. Their relative contribution percentages to the total mean dissipation (%) are shown in **e-h**. The relative contributions shown in **e-h** indicate that the summation of the top two sources can explain most ( $Pct_{1st} + Pct_{2nd} > 55\%$ ) of the total dissipation. GSP turbulence is the first largest contributor at low and mid latitudes in winter, and still the second largest contributor at high latitudes in both seasons.



766  
767  
768  
769  
770  
771  
772  
773  
774  
775  
776  
777

**Fig. 5 A schematic diagram of the four turbulence sources.** LSP, GSP, VBP, and AGSP represent the turbulence sources from Langmuir circulation, geostrophic current shear, vertical convection, and ageostrophic current shear. LSP is the shear to turbulence from Stokes drifts due to winds and waves. GSP is the shear to turbulence from geostrophic currents at fronts with down-front winds. VBP is the convection to turbulence by gravitational instability due to surface buoyancy loss. AGSP is the shear to turbulence from ageostrophic currents induced by winds. The left two pie charts show the spatial prevalence of each turbulence source in winter and summer, while the right two show the relative contribution of each source to the total dissipation magnitude averaged over the globe. These percentages indicate that GSP is a prevalent and significant source of OSBL turbulence over the globe.